

Advanced Models for Vibrational and Chemical Kinetics Applied to Mars Entry Aerothermodynamics

Iole Armenise*

Consiglio Nazionale delle Ricerche, 70126 Bari, Italy

Philippe Reynier†

Ingénierie et Systèmes Avancés, 33700 Mérignac, France

and

Elena Kustova‡

*St. Petersburg University,**198504, Saint Petersburg, Russia*

DOI: 10.2514/1.T4708

The paper presents a comparative study of vibrational-chemical kinetics and heat transfer in carbon dioxide flows under Mars entry conditions for two classes of models: the state-to-state and multitemperature models. The state-to-state approach treats each vibrational state of a molecule as a separate chemical species, thus providing a very detailed flow description. Reduced multitemperature models are based on nonequilibrium quasi-stationary Boltzmann distributions over vibrational energy with vibrational temperatures of different modes. Implementation of multitemperature models requires much less computational effort, making them rather attractive for engineering applications. Simulations have been performed for the upper part of the Mars Pathfinder entry trajectory. Comparisons between different models demonstrate a good agreement for the flowfield variables obtained using the state-to-state and multitemperature approaches, except some discrepancies for the species mole fractions prediction. This conclusion is encouraging for computational fluid dynamics, since it confirms that multitemperature models, while not being so much detailed as state to state, are still able to capture the main peculiarities of thermal and chemical nonequilibrium flows. The transport and thermochemical models have been validated using experimental data obtained in the NASA Hypersonic Pulse ground test facility. It is shown that both state-to-state and advanced multitemperature transport models used in the present simulations provide a better agreement for the heating predictions compared to traditional models.

Nomenclature

C_v	=	mass fractions of different species v
D	=	base diameter, m
D_{cd}	=	multicomponent diffusion coefficients, m^2/s
D_{Tc}	=	thermal diffusion coefficient of chemical species c , m^2/s
$D_{v_1, v_2, v_3, w_1, w_2, w_3}$	=	diffusion coefficients for different CO_2 vibrational states, m^2/s
$D_{w, v}$	=	diffusion coefficients for different vibrational states of diatomic molecules, m^2/s
d_c	=	diffusive driving force for c species, m^{-1}
d_v	=	diffusive driving forces for the vibrational state v of diatomic molecules, m^{-1}
$d_{v1, v2, v3}$	=	diffusive driving forces for the corresponding CO_2 vibrational states, m^{-1}
$E_{c, w}$	=	vibrational energy of diatomic species, J
E_{v_1, v_2, v_3}	=	vibrational energy of CO_2 molecule, J
$\langle E_{rot}^c \rangle$	=	mean rotational energy of c species, J
E^c	=	energy of formation, J
f	=	stream function
h	=	enthalpy, J/kg

k	=	Boltzmann constant, $J \cdot K^{-1}$
M	=	Mach number
n_c	=	molar fraction of species c
n_{cv}	=	molar fraction of species c in the corresponding vibrational state v
$n_{v1, v2, v3}$	=	molar fraction of CO_2 in the vibrational states v_1, v_2 , and v_3
Pr	=	Prandtl number
p	=	pressure, Pa
q	=	heat flux, W/m^2
q_{DVE}	=	heat flux due to diffusion of vibrational energy transferred by excited molecules, W/m^2
q_F	=	heat flux due to thermal conductivity (Fourier flux), W/m^2
q_{MD}	=	heat flux due to mass diffusion, W/m^2
q_{TD}	=	heat flux due to thermal diffusion, W/m^2
Re	=	Reynolds number
S	=	curvilinear abscissa, m
Sc	=	Schmidt number
S_T	=	source term of the energy equation in the boundary-layer equations
S_V	=	source terms of the continuity equations in the boundary-layer equations
T	=	temperature, K
t	=	time, s
V	=	velocity, m/s
V_c	=	diffusion velocities of atomic species, m/s
V_{cv}	=	diffusion velocity of species c on the vibrational level v , m/s
x	=	Cartesian abscissa, m
y	=	Cartesian ordinate, m
α	=	entry angle, deg
β	=	index of the residence time of a fluid element in a particular point of the domain, s^{-1}
η	=	self-similar Lees–Dorodnitsyn coordinate, with direction normal to the body surface

Received 23 February 2015; revision received 3 August 2015; accepted for publication 9 October 2015; published online 24 December 2015. Copyright © 2015 by the authors. Published by the American Institute of Aeronautics and Astronautics, Inc., with permission. Copies of this paper may be made for personal or internal use, on condition that the copier pay the \$10.00 per-copy fee to the Copyright Clearance Center, Inc., 222 Rosewood Drive, Danvers, MA 01923; include the code 1533-6808/15 and \$10.00 in correspondence with the CCC.

*Researcher, Instituto di Nanotecnologia, Via Amendola 122/D; iole.armenise@nanotec.cnr.it.

†Research Engineer, Bât O–Parc Cadéra sud, 12 rue Ariane; Philippe.Reynier@isa-space.eu.

‡Professor, Department of Mathematics and Mechanics, 28 Universitetskaya nab.; e.kustova@spbu.ru.

λ	=	heat conductivity coefficient of translational and rotational modes, W/m/K
θ	=	temperature normalized to the external temperature T_e
ρ	=	density, kg/m ³
ξ	=	self-similar Lees–Dorodnitsyn coordinate, with direction along the body surface
$\lambda_{v,12}, \lambda_{v,3}, \lambda_{v,c}$	=	heat conductivity coefficients of different vibrational modes, W/m/K
Subscripts		
c	=	chemical species: CO ₂ , CO, O ₂ , C, or O
e	=	external edge of the boundary layer
t	=	total conditions
v	=	vibrational states
w	=	wall
∞	=	freestream conditions

I. Introduction

MARS exploration programs, the interest in which was almost lost after several unsuccessful missions, are currently experiencing a revival. New missions are already started or in preparation; see [1,2] for the surveys of past and current missions to Mars. Preparation of a mission includes a huge amount of research work, both experimental and theoretical/numerical; in this framework, studies for physical-chemical kinetics and heat transfer under Mars entry conditions take an important place [3–5].

Mars's atmosphere consists of 95.32% carbon dioxide, 2.7% nitrogen, 1.6% argon, and a small amount of admixtures: oxygen, carbon monoxide, and water vapor. In Mars entry problems, there is a considerable increase in the amount of CO₂ dissociation products: CO and O. Therefore, for accurate predictions of fluid dynamic parameters, drag, and surface heat flux, it is necessary to take into account the peculiarities of CO₂ kinetics. Vibrational and chemical kinetics of polyatomic gases are much more complicated compared to that of the diatomic species. Several modes of vibrations create numerous relaxation channels; the rates of various relaxation processes may differ by several orders of magnitude. In this situation, the choice of appropriate kinetic model becomes of crucial importance.

The state-to-state model for high-temperature mixtures containing CO₂ was developed in [6–8]. The main peculiarity of the model is that it does not assume any quasi-stationary distributions over vibrational states; all vibrational transitions are considered at the macroscopic timescale. The model is very detailed and can provide a good understanding of relaxation and transport processes. On the other hand, its implementation requires high computational costs; currently, the state-to-state model cannot be applied to two-dimensional (2-D) and three-dimensional (3-D) simulations for a real lander entering the Mars atmosphere. This model has been implemented to a one-dimensional (1-D) boundary-layer (BL) code simulating the flow along the stagnation line [7–11].

Multitemperature models are based on splitting the relaxation mechanisms to fast and slow, depending on the rates of vibrational transitions and chemical reactions. There is a great variety of multitemperature models, starting from the simplest one [12] assuming a unique vibrational temperature for all vibrational modes toward more accurate models introducing vibrational temperatures for each mode of vibrations [13,14] and taking into account anharmonic effects [15–18]. The models developed in [13,14] were applied in [19,20] for simulations of a Mars sample return orbiter. They were also implemented in the TINA computational fluid dynamics (CFD) code [21].

The objective of the present study is to compare solutions obtained by means of the state-to-state and multitemperature models and validate them against available experimental data. The present contribution focuses on the numerical study of a five-component CO₂/CO/C/O/O₂ mixture flow near the blunt-body model adopted in the NASA Hypersonic Pulse (referred to as HYPULSE) expansion tube [22,23] and around the Mars Pathfinder probe during early stages of its entry. We compare the macroscopic variables calculated using boundary-layer and TINA codes, as well as the surface heat flux

obtained numerically and measured by Hollis and Perkins [22,23] in the HYPULSE facility. In this way, we can specify the limits of applicability for the state-to-state and multitemperature models.

The choice of test cases is based on the thorough analysis performed in [1]. We rebuild numerically some points of the Mars Pathfinder trajectory before peak heating since transition to turbulence occurs 7 s after peaking conditions. To these points, we add a case for which experimental results are available and representative of Mars entry conditions. Since the work carried out in ONERA F4 hot-shot and DLR HEG shock-tunnel for three ESA ExoMars mission development has highlighted some uncertainties in the freestream conditions as well as a high level of CO₂ dissociation [24], we decided to rebuild the test performed in the HYPULSE facility for the Mars Pathfinder. The point selected is the test run in HYPULSE with pure CO₂ at a velocity of 4.788 km/s.

The entry trajectory has already been reconstructed using CFD calculations. This allows some comparisons with other numerical simulations. The numerical reconstruction performed by Milos et al. [25] has been, so far, the most extensive postflight aerothermodynamics analysis done with the flight data. These authors investigated the entry trajectory of the Mars Pathfinder using the NASA GIANTS CFD code that solves the nonequilibrium Navier–Stokes equations. The chemical kinetics used for the calculations were those retained for the mission preparation [26]. Since the catalyticity of SLA-561 TPS material was not determined, a conservative approach was selected, allowing only CO₂ formation and excluding O₂ formation. Calculations showed that assuming a noncatalytic surface results in at least a 60% reduction in heating compared to the fully catalytic case. A fully catalytic model has been retained for the postflight rebuilding.

Another effort for the use of the flight data was carried out by Paterna et al. [27], who performed an experimental and numerical study on Mars Pathfinder entry. Numerical computations of the peak heating conditions were carried out for noncatalytic and fully catalytic conditions. The results for the heating rates were compared to the flight data [25]. Recently, Surzhikov and Omaly [28,29], in supporting the European ExoMars project (and more particularly, the assessment of the radiative heating), performed a rebuilding of the Pathfinder entry. The thermochemistry effects were accounted for through a 10-species model (C, N, O, C₂, N₂, O₂, CN, CO, NO, CO₂) and a pseudocatalytic surface. Radiative heating was determined using a ray tracing method. However, no comparison was performed against the Pathfinder flight data or numerical and experimental predictions.

The paper is organized as follows. First, we discuss briefly the macroscopic models used in simulations. We introduce the state-to-state model and specify its peculiar features for flows containing CO₂; the kinetic scheme and the transport model are described in Sec. III.A. A multitemperature flow description is introduced in Sec. III.B. After that, we give details on the computational tools: in Sec. III.C, the code for simulation of a state-to-state 1-D flow along the stagnation line is considered, and then the TINA CFD code used in multitemperature simulations is described in Sec. III.D. The results and discussion are given in Secs. IV and V. We compare the results obtained for the conditions of Hollis and Perkins's experiments [22,23] in the HYPULSE facility: the calculations have been performed in the frame of multitemperature and state-to-state models using CFD and BL codes, and the heat flux calculated in different approaches is compared with that measured by Hollis and Perkins. In Sec. V, the results of flow reconstruction for several points of the Mars Pathfinder trajectory that were carried out using the TINA CFD code with different thermochemical models are presented. Concluding remarks are given in Sec. V.

II. Flow Models and Computational Tools

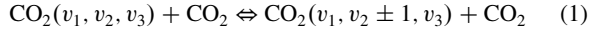
A. State-to-State Model

The state-to-state flow description is valid when the characteristic times of all vibrational energy transitions are of the same order as those for chemical reactions and comparable to the gas-dynamic time for the flow variable change. In the state-to-state model, by “species” we mean each vibrational state of each molecule as well as each atom. In our mixture, we have 47, 68, and 1224 species for O₂, CO, and CO₂ vibrational levels, respectively; and two atomic species: C and O. For

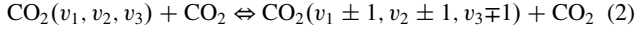
CO₂ molecules, the vibrational states take into account all the possible combinations of the vibrational modes: symmetric stretching, degenerated bending, and asymmetric stretching mode. To be precise, the number of CO₂ states is 9018, but we reduced it by approximating the CO₂ dissociation energy to 3 eV instead of 5.5166 eV to reduce the computational cost of our code. Details are given in [7].

The vibrational and chemical kinetic processes taken into account in the present model are the following:

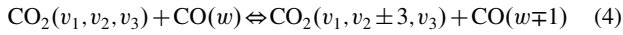
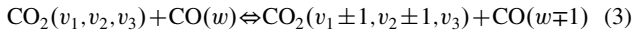
Vibrational-translational VT₂ transitions in the bending mode:



Inter-mode VV₁₋₂₋₃ exchanges within the CO₂ molecule:



Inter-mode VV_{m-k} exchanges between molecules of different chemical species, VV_{1-2-CO} and VV_{2-CO}:



Dissociation–recombination reactions, with M = CO₂, CO:



All these processes are taken into account in the equations of vibrational-chemical kinetics.

1. State-to-State Transport Model

The state-to-state transport theory for mixtures containing CO₂ and N₂ is developed in [6] and generalized for the five-component mixture in [7]. In a considered mixture, the expression for the heat flux has the form

$$\begin{aligned} \mathbf{q} = & -\lambda \nabla T - p \sum_c D_{Tc} \mathbf{d}_c \\ & + \sum_{v_1 v_2 v_3} \left(\frac{5}{2} kT + \langle E_{\text{rot}}^{\text{CO}_2} \rangle + E_{v_1 v_2 v_3} + E^{\text{CO}_2} \right) n_{v_1 v_2 v_3} \mathbf{V}_{v_1 v_2 v_3} \\ & + \sum_{c=\text{CO}, \text{O}_2} \sum_w \left(\frac{5}{2} kT + \langle E_{\text{rot}}^c \rangle + E_{c,w} + E^c \right) n_{c,w} \mathbf{V}_{c,w} \\ & + \sum_{c=\text{C}, \text{O}} \left(\frac{5}{2} kT + E^c \right) n_c \mathbf{V}_c \end{aligned} \quad (6)$$

where n_{cv} is the molar fraction of species c in the corresponding vibrational state v , $\lambda = \lambda_{\text{tr}} + \lambda_{\text{rot}}$ is the heat conductivity coefficient of translational and rotational degrees of freedom, p is the pressure, D_{Tc} is the thermal diffusion coefficient of chemical species c ($c = \text{CO}_2, \text{CO}, \text{O}_2, \text{C}, \text{O}$), \mathbf{d}_c is the diffusive driving force for c species, E_{v_1, v_2, v_3} is the vibrational energy of CO₂ molecule, $E_{c,w}$ is the vibrational energy of diatomic species, $\langle E_{\text{rot}}^c \rangle$ is the mean rotational energy of c species, E^c is the energy of formation, k is the Boltzmann constant, and T is the temperature.

The diffusion velocities \mathbf{V}_c of the atomic species have the classical form

$$\mathbf{V}_c = -\sum_d D_{cd} \mathbf{d}_d - D_{Tc} \nabla \ln T \quad (7)$$

(D_{cd} are the multicomponent diffusion coefficients), whereas $\mathbf{V}_{v_1, v_2, v_3}$ and $\mathbf{V}_{c,w}$ depend on the vibrational states

$$\begin{aligned} \mathbf{V}_{v_1, v_2, v_3} = & -\sum_{w_1, w_2, w_3} D_{v_1, v_2, v_3, w_1, w_2, w_3} \mathbf{d}_{w_1, w_2, w_3} - \sum_{d \neq \text{CO}_2} D_{cd} \mathbf{d}_d \\ & - D_{T_{\text{CO}_2}} \nabla \ln T \end{aligned} \quad (8)$$

$$\mathbf{V}_{c,w} = -\sum_v D_{w,v} \mathbf{d}_{cv} - \sum_{d \neq c} D_{cd} \mathbf{d}_d - D_{Tc} \nabla \ln T \quad (9)$$

where $D_{v_1, v_2, v_3, w_1, w_2, w_3}$ and $D_{w,v}$ are the diffusion coefficients for different vibrational states of CO₂, O₂, and CO; and $\mathbf{d}_{v_1, v_2, v_3}$ and \mathbf{d}_v are the diffusive driving forces for the corresponding vibrational states depending on the gradients of n_{v_1, v_2, v_3} and n_v .

As it is seen, in the state-to-state approach, the heat flux and diffusion velocities depend on the gradients of all level populations, atomic number density, gas temperature, and pressure. The total heat flux can be represented as a sum of several contributions [7]:

$$\mathbf{q} = \mathbf{q}_F + \mathbf{q}_{\text{MD}} + \mathbf{q}_{\text{TD}} + \mathbf{q}_{\text{DVE}} \quad (10)$$

where \mathbf{q}_F is the heat flux caused only by thermal conductivity (the Fourier flux); \mathbf{q}_{MD} and \mathbf{q}_{TD} are the fluxes caused by mass and thermal diffusion; and \mathbf{q}_{DVE} is the flux due to diffusion of vibrational energy transferred by excited molecules. Although the terms \mathbf{q}_F , \mathbf{q}_{MD} , and \mathbf{q}_{TD} appear in all commonly used definitions of the heat flux, the last term (\mathbf{q}_{DVE}) is a characteristic feature of the state-to-state model, since it is specified by the gradients of the vibrational level populations.

B. Multitemperature Model

The computational cost of the state-to-state model and, in particular, of the state-to-state transport model is extremely high. Although it is still acceptable to simulate a 1-D flow, it can be hardly implemented into 2-D and 3-D codes. Consequently, it is necessary to develop and validate reduced models, like multitemperature ones, which are more appropriate for implementation into 2-D and 3-D codes.

The multitemperature flow description is based on the assumption that a part of the vibrational energy transitions proceeds much faster than chemical reactions. The populations of vibrational states therefore follow the nonequilibrium Boltzmann or Treanor distributions with vibrational temperatures associated to different vibrational modes [13,14]. The set of flow variables is greatly reduced compared to the state-to-state model and consists of mass fractions of chemical species, velocity, temperature, and temperatures of different vibrational modes. Governing equations include equations of multitemperature chemical kinetics, conservation equations of mass, momentum and total energy, and relaxation equations for specific vibrational energies of different modes.

The transport properties in the multitemperature model are considered in detail in [13,14]. Thus, the vibrational energy flux \mathbf{q}_{DVE} in this case can be expressed in terms of vibrational temperature gradients and corresponding heat conductivity coefficients:

$$\mathbf{q}_{\text{DVE}} = -\lambda_{v,12} \nabla T_{12} - \lambda_{v,3} \nabla T_3 - \sum_{c=\text{CO}, \text{O}_2} \lambda_{v,c} \nabla T_{v,c} \quad (11)$$

Here, T_{12} and T_3 are, respectively, vibrational temperatures of combined symmetric-bending and asymmetric CO₂ modes; $T_{v,c}$ are vibrational temperatures of diatomic species; and $\lambda_{v,12}$, $\lambda_{v,3}$, and $\lambda_{v,c}$ are vibrational heat conductivity coefficients. The remaining terms in the heat flux are calculated similar to the case of state-to-state model.

Algorithms for the calculation of all transport coefficients in the multitemperature approach are proposed in [13,14]. For the present study, these algorithms are implemented directly into the CFD solver TINA [30], and no postprocessing is required for the heat flux calculation in the multitemperature model.

C. Boundary-Layer Code

To deeply analyze the boundary-layer region, we use a boundary-layer code (BL), that couples fluid dynamics and state-to-state vibrational-chemical kinetics. This code was developed and validated by Armenise and Kustova in earlier papers [7,8]. The fluid dynamics is really simplified; indeed, boundary-layer equations are written in self-similar Lees–Dorodnitsyn coordinates (ξ, η), and therefore the problem is reduced to a 1-D one in the direction η normal to the body surface [31]. On the opposite, the vibrational-chemical kinetics is very detailed. The equations discretized and solved in the BL code are

$$\frac{\partial^2 C_v}{\partial \eta^2} + f Sc \frac{\partial C_v}{\partial \eta} = S_v, v = 1, \dots, NumSp \quad (12)$$

$$\frac{\partial^2 \theta}{\partial \eta^2} + f Pr \frac{\partial \theta}{\partial \eta} = S_T \quad (13)$$

The first $NumSp$ equations are the continuity equations of each species and, in the present model, for what stated in Sec. III.A, $NumSp = 1341$. The last equation is the energy equation. In the source terms on the right-hand sides of Eqs. (12) and (13), the vibrational and chemical kinetic processes [Eqs. (1–5)] are included. The macroscopic variables are $C_v = \rho_v/\rho$ (mass fractions of different species) and $\theta = T/T_e$ (temperature normalized to the external temperature T_e). The stream function is f ; and Sc and Pr are the Schmidt and Prandtl numbers, respectively, that are here fixed to the values $Sc = 0.49$ and $Pr = 0.71$: the limit in using constant Schmidt and Prandtl numbers has been studied in [8].

The boundary conditions to be set are those at the external edge of the boundary layer and on the surface. At the external edge, we specify temperature T_e ; pressure P_e ; species mass fractions (the molecular vibrational distributions are chosen as Boltzmann at T_e); and, finally, the parameter $\beta = du_e/dx$, which is an index of the residence time of a fluid element in a particular point of the domain. On the surface, we set the wall temperature T_w and, to simulate a noncatalytic wall, the zero mass fraction derivatives

$$(\partial C_v / \partial y)_w = 0 \quad (14)$$

Finally, the BL code solves the boundary-layer equations (12) and (13) with the finite difference method on a uniform grid of 80 nodes, using an iterative approach up to the convergence.

It is worth mentioning that calculation of the state-to-state diffusion velocities and heat flux based on the exact formulas of kinetic theory [Eqs. (6–9)] is extremely time consuming. Therefore, in the BL code, we use a postprocessing procedure: first, we calculate the flowfield using simplified equations [Eqs. (12) and (13)] and, as the next step, we calculate the transport coefficients and the heat flux using the kinetic theory algorithms proposed in [6].

D. CFD Solver

The tool used for CFD is TINA [21]. TINA is a message-passing interface parallel multiblock 3-D finite volume, thermochemical, nonequilibrium two-phase Navier–Stokes code developed by Fluid Gravity Engineering, Ltd., initially as a research code, but which has also been used in design studies over the years. The numerical scheme is based on the Roe scheme with the flux limiter proposed by Yee [32]. The time-stepping marching is carried out with an implicit time algorithm. The solver is second-order accurate in space and first order in time. TINA can handle different physical and chemical phenomena, like chemical and thermal nonequilibrium. The code has a choice of one-, two-, three-, or multitemperature models, as well as a full nonequilibrium chemical kinetics model. The thermochemistry is coupled with the Navier–Stokes equations in an implicit way, which gives superior convergence characteristics compared with loosely coupled solutions; and relaxation of the source terms is available.

In addition, the code has the capability to simulate turbulence, two-phase flows with particle tracking, catalysis and ablation, flows where electronic relaxation, catalytic surfaces, ablation, external radiation and multiphase effects. TINA is used primarily for supersonic/hypersonic Navier–Stokes calculations where nonequilibrium thermochemistry modeling is required. A total-variation-diminishing shock-capturing algorithm [32] is used, which ensures nonoscillatory behavior near shock waves at essentially any freestream Mach number.

To handle the different mentioned features, TINA has a number of boundary conditions that can be applied, including catalysis and ablation. These boundary conditions are modular; thus, it is not

difficult to implement new boundary condition modules into the code. TINA has a choice of relaxation models: the Park two-temperature model, the three-temperature model allowing separate electron temperatures, and the multivibrational temperature model. Chemical kinetics are modeled with a standard generalized Arrhenius form with a selection of appropriate temperature weighting.

Transport properties are based around viscosity curve fits for each species. The mixture viscosity is calculated from the individual species viscosities using Wilke's mixing rule [33]. Diffusion coefficients are computed from viscosity and Schmidt numbers. Thermal conductivity coefficients are calculated using the Eucken relation. First, the species viscosity is computed using Blottner et al.'s curve fits [34]. Then, more complex models have been tested: CFD calculations with a multitemperature model derived from a state-to-state model, and a full state-to-state approach.

TINA has been in use at the European Space Research and Technology Centre since 1991, and most recently was used in supporting the Huygens coupled radiation studies [35]. During the time period of 1991–1996, several catalytic and ablation models were incorporated. The initial studies of catalysis for Mars entry were undertaken in 1994, moreover the code was recently used for supporting ExoMars mission preparation [24]. Coupled ablation radiation studies were also undertaken for high-speed Earth return [36,37]. Several turbulence models were also available.

III. HYPULSE Test Reconstruction

The test model used for the experiments conducted in the HYPULSE facility [22,23] was made with Macor, which is a ceramic with a low catalytic efficiency; it was maintained by a sting in steel and equipped with thin-film gauges for measuring the heating. The geometry of the test model used in HYPULSE is shown in Fig. 1: the different parameters for the sphere cone are $R_n - 0.5$ in., $R_b/R_n = 2$, $R_a/R_n = 1.2$, $R_n/R_c = 10$, and $L/R_n = 1.723$. The test conditions in terms of velocity and freestream conditions are the following: velocity is 4788 m/s, density is 5.738×10^{-3} kg/m³, pressure is 1182 Pa, and temperature is 1090 K.

The experiments were numerically rebuilt earlier [38–40] using noncatalytic conditions and a wall temperature of 300 K, showing a good qualitative agreement for the heat flux. For the modeling of nonequilibrium thermochemical effects, the eight-species (CO_2 , CO , N_2 , O_2 , NO , C , N , O) model proposed by Candler [41] was retained. In the present paper, we use thermochemical models described in the next sections.

A. CFD Numerical Predictions

Axisymmetric computations were performed using TINA for the conditions reported previously. Several meshes were tested for checking the grid dependence of the results. The first meshes with 80×80 cells were found to be a little bit coarse to ensure a good convergence and a good capture of the shock (both are linked, in fact).

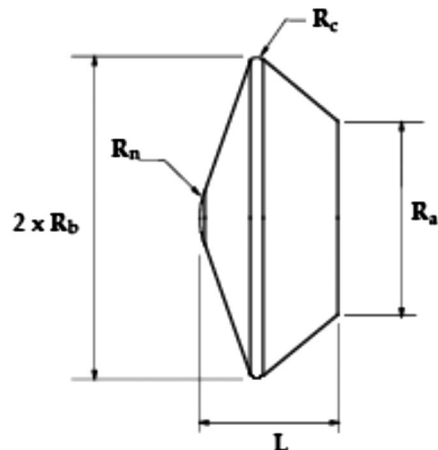


Fig. 1 Model tested in the HYPULSE facility [22].

Finally, an 80×100 -cell mesh was found adequate, since a finer mesh with 200×200 cells did not improve the results. The computational domain extends over 3 mm along the stagnation line with a first cell at the wall of $3 \mu\text{m}$ in order to have a good accuracy when predicting the heating rate. The computational mesh is shown in Fig. 2.

The calculations have been carried out for an isothermal wall at 300 K, since this is the room temperature at the beginning of the test that has a short duration of less than $300 \mu\text{s}$ [40]. The model was inserted at this temperature in the tunnel, and the test duration was short. As a consequence, this temperature has been retained for the calculations. The results have been converged with 120,000 iterations; and time steps were in between 0.1 and 1 times the Courant–Friedrichs–Lewy (CFL) number. The assumption of a laminar flow has been made, as was already done for the reconstruction of the experiments [39].

A noncatalytic wall was retained for the calculations, since the Macor has a low catalytic efficiency; however, one simulation was performed for a fully catalytic wall. At first, the nonequilibrium thermochemical effects were accounted through the model with five species (O_2 , CO , CO_2 , C , O) and five reactions proposed by Park et al. [42]. The first transport model based on the Blottner et al.'s curve fits [34] and Wilke's mixing rule [33] is described in Sec. II.D. Then, more complex models were tested. A second set of calculations was carried out, still using Park et al.'s model [42] for the chemical reactions, but the transport properties were calculated on the basis of the CO_2 model proposed by Kustova and Nagnibeda [13], which were adapted to two-temperature calculations. Finally, the collisional-radiative model proposed by Bultel [43] with 16 species

(and related excitation levels) and 67 reactions was tested with a Blottner et al. approach [34] for the transport properties.

B. Results Obtained with the Park Model

Calculations have been carried out using the Park et al. model [42] for a noncatalytic wall at 300 K. The flowfield distributions of the temperature and species mole fractions are plotted in Figs. 3–6. The results show that the level of translational temperature reaches a maximum of 9900 K in the shock layer, whereas the vibrational temperature maximum is lower at 6600 K (see Fig. 3). This difference has already been identified in previous computations [44] carried out with different thermochemistry models, as well as in a shock wave study with a direct simulation Monte Carlo method [45]. The mole fractions of CO_2 and CO are displayed in Fig. 4. As expected, CO_2 is dissociated in the shock layer, which is translated by the high fraction of CO there. The maximum of the CO mole fraction is located at the frustum, where there is less energy available for its dissociation.

This point is consistent with Fig. 5, where the mole fractions of O_2 and O are plotted. The mole fraction of O_2 is higher in the region of the shock layer located near the shoulder due to the lower level of energy available. In Fig. 6, the mole fraction of C is displayed. The figure highlights that a low level of atomic carbon is present at the shock location.

The distributions of the vibrational and translational temperatures along the stagnation line are plotted in Fig. 7. The curves show the presence of thermal nonequilibrium at the shock location. The thermal nonequilibrium zone extends over 0.2 mm, and the shock standoff is 1 mm. In the right part of the same figure, the heat-flux distributions computed through different approaches are plotted. Calculations have been carried out using the Park et al. model [42] with Blottner's [34] and Kustova and Nagnibeda's [13] approaches for the transport properties. The heating has been also computed for a full catalytic wall using Blottner coefficients [34]. The numerical predictions show a huge difference between noncatalytic and catalytic predictions: approximately 6 MW/m^2 instead of nearly 15 MW/m^2 . The noncatalytic predictions are closer to the experimental values at the stagnation point, which is around 8 MW/m^2 , as shown in [22]. This confirms the weak catalyticity of the Macor and, as a consequence, all other calculations have been performed for noncatalytic walls.

C. Advanced Models

Calculations carried out with the different transport models (while the chemical kinetics are the same) lead to similar flowfield distributions of the fluid-dynamic variables. In Fig. 8, the distributions of translational and vibrational temperatures predicted using Kustova and Nagnibeda's [13] thermal properties are plotted. The flowfield pattern of these quantities is similar to those plotted in Fig. 3. The distributions are nearly the same and, for both calculations, the maximum of the translational and vibrational

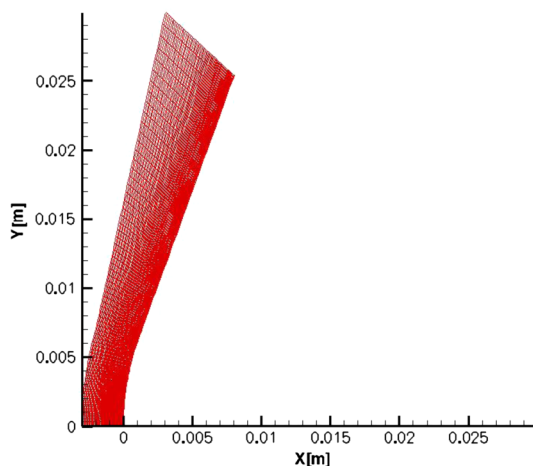


Fig. 2 Computational grid.

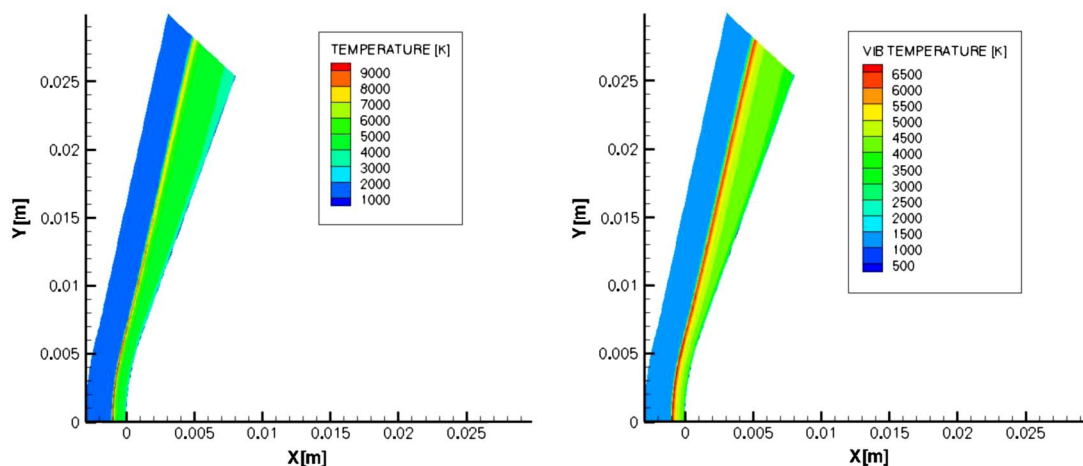


Fig. 3 Distributions of translational and vibrational (VIB) temperatures (left and right, respectively).

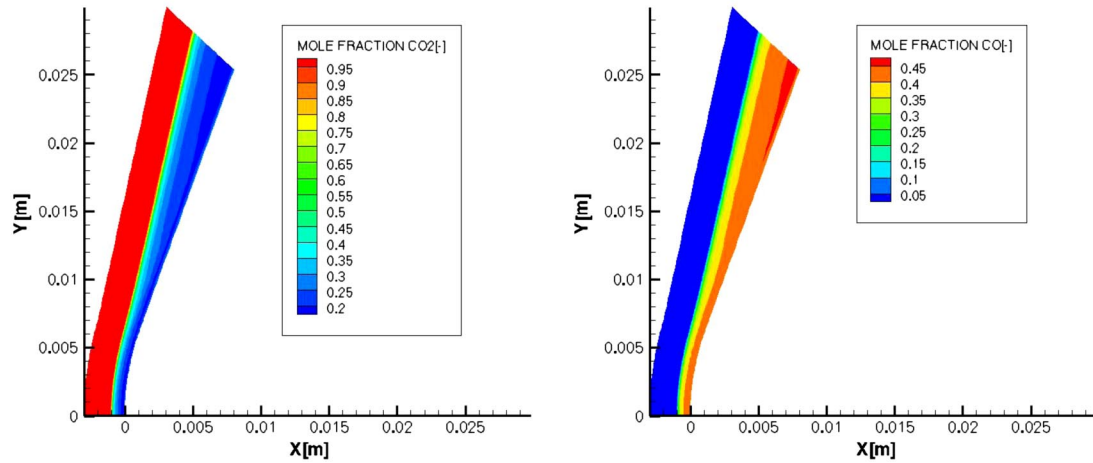


Fig. 4 Distributions of CO_2 and CO mole fractions (left and right, respectively).

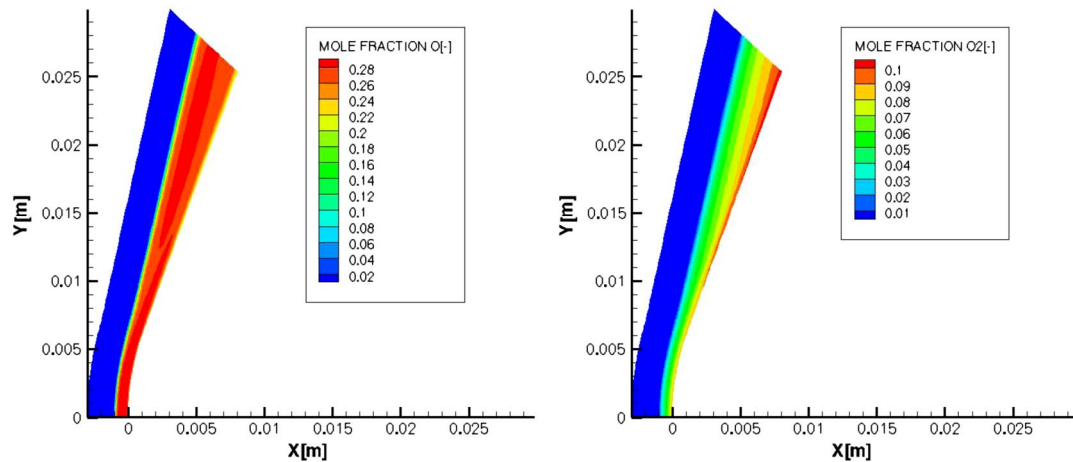


Fig. 5 Distributions of O and O_2 mole fractions (left and right, respectively).

temperatures reaches values of 9900 and 6860 K, respectively. These small differences (when comparing to the results of Fig. 3) in the maximum values of the temperature are due to the different model used for the transport properties. Some differences have also been highlighted when comparing the calculations performed with the collisional-radiative model [43]. In this last case, since Blottner et al.'s modeling [34] is used for the transport properties, differences are induced by the reacting scheme.

The temperature distributions computed using this model are displayed in Fig. 9. The flowfield patterns of the temperatures look like those plotted in Fig. 3 and in Fig. 7. However, the temperature maximums are here lower than for the calculations performed with the Park et al. model [42]. This is confirmed by the values of the maxima. The translational temperature is lower than 9300 K, whereas the vibrational temperature is lower than 6300 K. Comparing to the previous values of 9900 and 6860 K, a decrease of 600 K can be observed. Since the transport properties are computed using the same model, this difference is due to the different reacting scheme. In the Bultel model [43], the C_2 is included in the species and some excited states for C_2 and CO are considered. The change of the reacting scheme, accounting for other species and different excited levels, has, of course, some influence on the species and temperature distributions. A dedicated effort would be required to have a deeper analysis, which is beyond the objectives of the current study.

The predicted heat-flux distributions have been compared with the experimental data in Fig. 10. The values predicted using the model proposed by Bultel [43] have not been reported in this figure, since the stagnation point heat flux of 6.3 MW/m^2 is the same as the value predicted using Park et al.'s [42] model (with Blottner coefficients). This is due to the fact that the surface heating depends strongly on the modelling of the transport properties. Here, since the Blottner model

is used for both calculations, a similar value for the heating could be expected. The heat flux predicted using the Blottner approach underestimates the values computed using the Kustova and Nagnibeda [13] model. The respective values at the stagnation point are 6.3 and 6.8 MW/m^2 . Both values underestimate the experimental data of 8 MW/m^2 by 22 and 15%, respectively. However, the prediction provided by the Kustova model is in the experimental uncertainty range of the stagnation point heating indicated in [38]. Additionally, the predictions done with the Kustova model are in good agreement with the experimental data along the surface, whereas the Blottner coefficients underestimate the

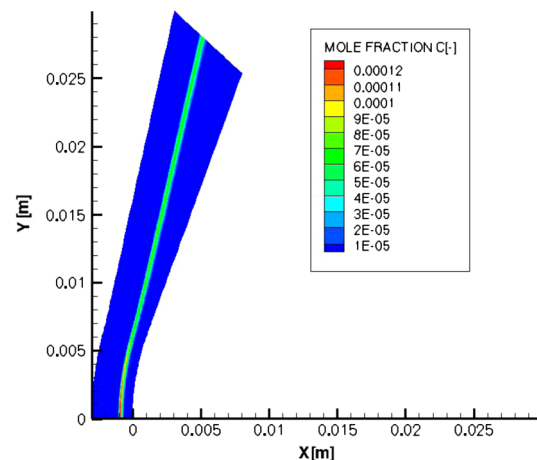


Fig. 6 Distribution of C mole fraction.

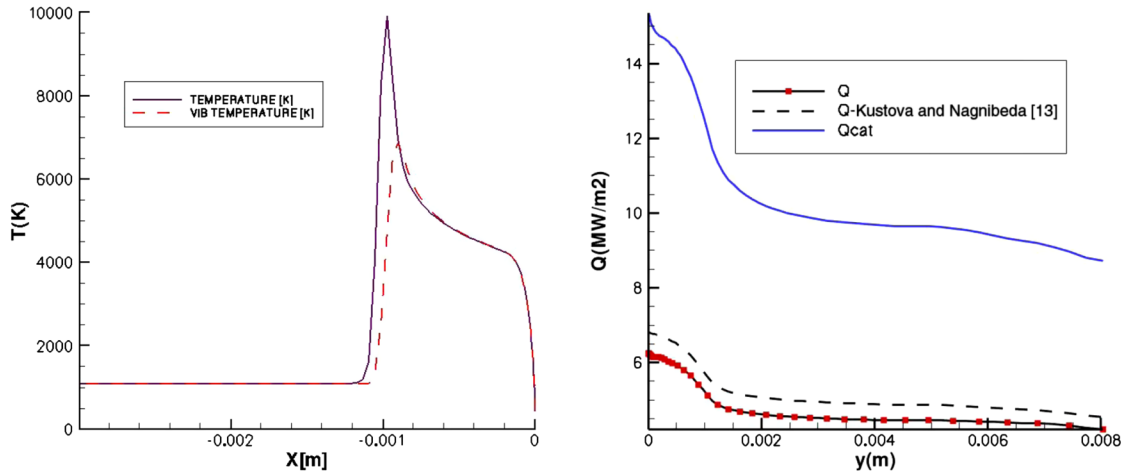


Fig. 7 Stagnation line distributions of translational and vibrational temperatures (left), and distributions of heating over the surface (right; y is the spanwise direction).

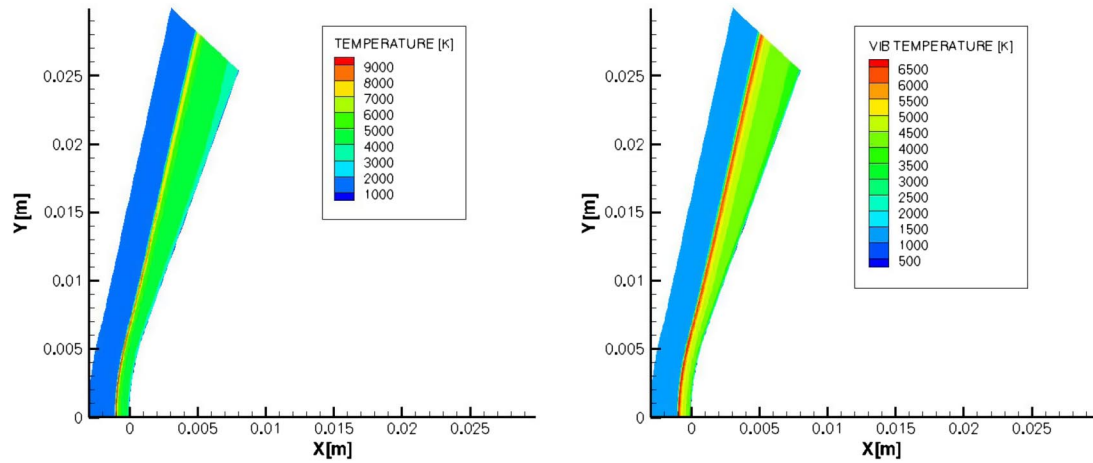


Fig. 8 Distributions of translational and vibrational temperatures (left and right, respectively) predicted using Kustova and Nagnibeda's [13] thermal properties.

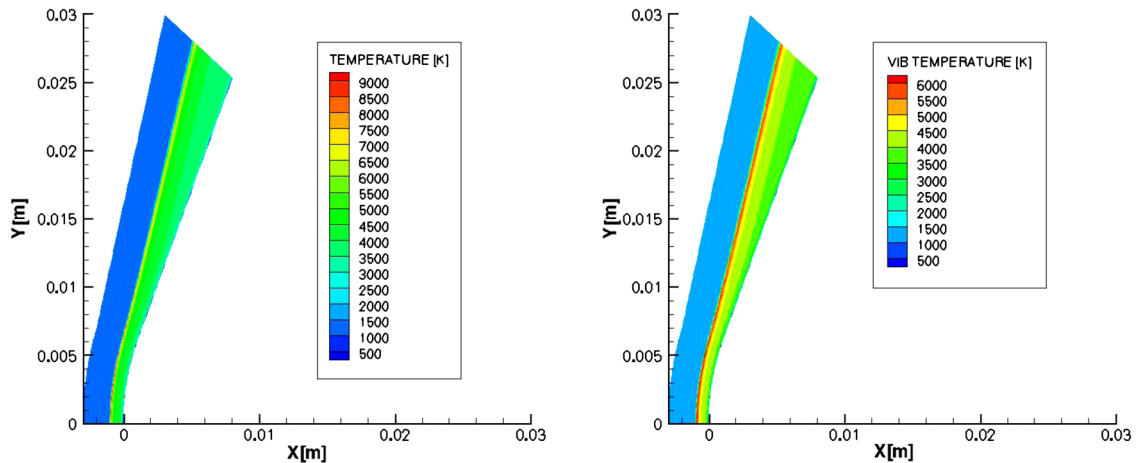


Fig. 9 Distributions of translational and vibrational temperatures (left and right, respectively) predicted using the collisional-radiative model [43].

experiments. The difference is apparently due to the different models used for computing the transport properties. This is pointed out in Fig. 11, in which the flowfields of the dynamic viscosity are plotted. If the general shapes of the figures are similar, the Kustova model leads to viscosity levels slightly higher than the standard Park et al. model [42]. This difficulty to recover the convective heating for Mars entries has already been pointed out for the numerical reconstruction of Mars Science Laboratory entry [46].

D. State-to-State Model Results and Comparison with CFD Results

To compare results obtained in the boundary layer with the multitemperature and state-to-state models (i.e., by running our two codes), it is necessary to work under analogous conditions. Hence, to set the boundary conditions of the BL code, which simulates the state-to-state flow, we choose the results obtained by solving the 2-D problem using TINA with its multitemperature model, as explained in Secs. II.B and II.D. We consider a five-species $CO_2/CO/C/O/O_2$

mixture and a noncatalytic wall. The freestream conditions are reported in Table 1. The test case corresponding to the experiment of Hollis and Perkins [22,23] is referred to as test case 1 (HYPULSE).

Analyzing the temperature profile obtained with the TINA code under the conditions mentioned previously (which is almost equal to the one of Fig. 7), we conclude that it is reasonable to fix the boundary-layer thickness at around 4.1×10^{-4} m, where the temperature curve reaches an almost constant value behind the inflection point close to the surface. In the 1-D boundary-layer problem, the distance is counted from the surface toward the external edge; the value of 4.1×10^{-4} m corresponds to -4.1×10^{-4} m in the 2-D problem. In the BL calculation, the external edge boundary conditions are therefore set using the values calculated at $x = -4.1 \times 10^{-4}$ m by solving the 2-D problem with TINA; the value of the input parameter β is calculated for a nose radius of 1.27×10^{-2} m (see Fig. 1).

Let us discuss first the results obtained under conditions of the Hollis and Perkins experiment [22,23] (test case 1 HYPULSE). In our simulations, using the BL code, the wall temperature T_w has been fixed to 700 K and not to 300 K as in TINA calculation in order to increase the numerical scheme stability.

In Fig. 12, the species molar fractions as well as the total density along the stagnation line in the boundary-layer region are reported; curves 1 correspond to the multitemperature model, implemented in TINA; and curves 2 correspond to the state-to-state one, implemented in the BL code. The values at $X = 4.1 \times 10^{-4}$ m coincide due to the external boundary conditions chosen in the BL code. In the boundary

Table 1 Boundary conditions and input parameters adopted in test cases run with the BL code

Variable	Test case 1 HYPULSE	Test case 2	Test case 3	Test case 4
T_w	700 K	700 K	1500 K	1500 K
T_e	4555 K	4555 K	6000 K	6000 K
P_e	1.269×10^5 Pa	888 Pa	1.269×10^5 Pa	888 Pa
β	1.283×10^5 s $^{-1}$	2708 s $^{-1}$	1.283×10^5 s $^{-1}$	2708 s $^{-1}$
(O $_2$ + O)%	35.7835	35.7835	35.7835	35.7835
O $_2$ %	5.6685	5.6685	5.6685	5.6685
O%	30.115	30.115	30.115	30.115
CO $_2$ %	22.6662	22.6662	22.6662	22.6662
CO%	41.5502	41.5502	41.5502	41.5502
C%	1.0×10^{-4}	1.0×10^{-4}	1.0×10^{-4}	1.0×10^{-4}

layer, the species mole fractions depend considerably on the model. In particular, in the state-to-state model, the dissociation rate depends on the populations of different vibrational levels, which in turn depend on the other kinetic processes; whereas in the multitemperature models the vibrational ladder is not detailed. The maximum differences are found for the O, C, and CO $_2$ species on the surface: the O mole fraction is 0.2537 when it is calculated with the multitemperature model and 0.0967 when calculated with the state-to-state one, showing a discrepancy of more than one order of magnitude; the C mole fraction is 9.7921×10^{-24} if calculated with the multitemperature model and 1.3870×10^{-6} if calculated with the state-to-state one; and finally, the CO $_2$ mole fraction is 0.2416 if calculated with the multitemperature model and about twice this value (i.e., 0.4317) if calculated with the state-to-state one. These differences should be due to the two models adopted more than the different temperature fixed on the surface; indeed, a quick estimation of mole fractions obtained with the state-to-state model and a wall temperature of $T_w = 300$ K gives only slightly different values with respect to test case 1, in which $T_w = 700$ K.

The total density along the stagnation line calculated with the two models is plotted in Fig. 12f; one can notice an excellent agreement. Along the stagnation line, one can notice an excellent agreement.

In Fig. 13, the viscosities calculated with TINA, with Kustova and Nagnibeda's model [13,14], and with the 1-D BL code are plotted along the stagnation line. The agreement obtained using two models is very good: the most important difference is on the surface, where the viscosity calculated with the multitemperature model is 2.39×10^{-5} Pa s, whereas the viscosity calculated with the state-to-state model is 3.34×10^{-5} Pa s. This discrepancy is due to the wall temperature difference; the values of species molar fractions on the surface obtained with the wall temperatures of 300 and 700 K are very close, and their variation practically does not change the viscosity coefficient. Moreover, we have found that nonequilibrium vibrational distributions of the molecules do not affect the shear viscosity coefficient.

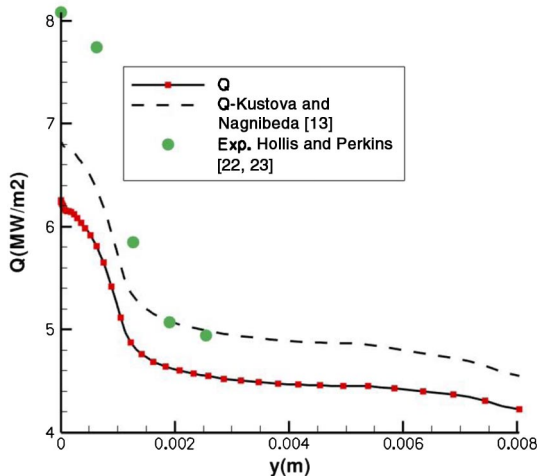


Fig. 10 Heat-flux distributions predicted using Blottner et al.'s [34] and Kustova and Nagnibeda's [13] thermal properties and experimental data.

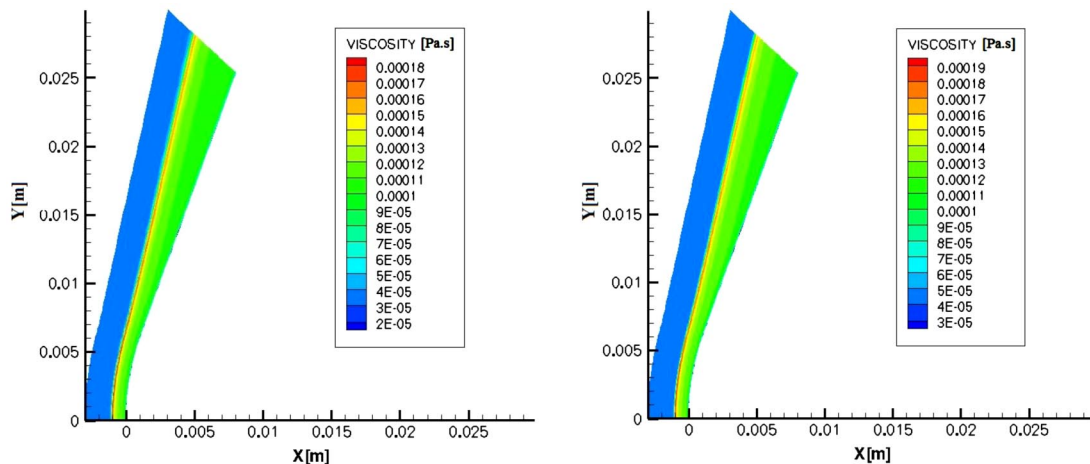


Fig. 11 Distributions of viscosity predicted using Blottner et al.'s [34] and Kustova and Nagnibeda's [13] thermal properties (left and right, respectively).

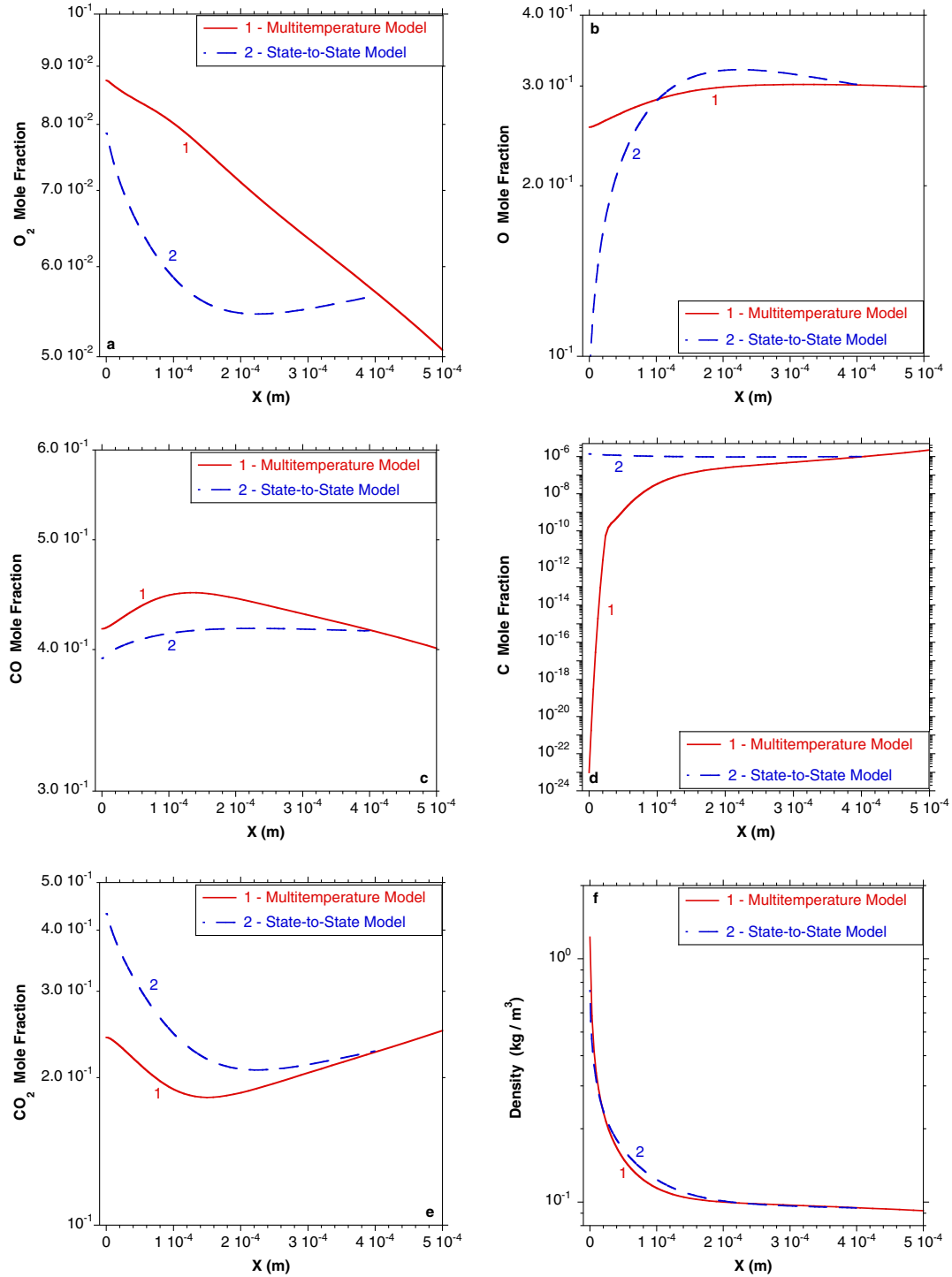


Fig. 12 Species molar fractions and total density obtained with different models.

In Fig. 14a, we compare the enthalpy per unit mass calculated in the boundary layer using our two models. First, the negative enthalpy values close to the surface can be explained by the negative values of the CO_2 and CO formation energies. The second, more important observation is that, although the trend is the same, the enthalpy calculated using the multitemperature model incorporated in TINA is higher than that calculated with the state-to-state model (BL code). In particular, at the edge of the boundary layer, the enthalpy per unit mass calculated with the multitemperature model is 3.39 MJ/Kg, whereas the one calculated with the state-to-state model is 1.87 MJ/Kg. If we retain in our calculations all 9018 CO_2 vibrational states corresponding to the full model [7], we obtain the enthalpy per unit mass of 2.03 MJ/Kg. Therefore, the reason for underestimated

enthalpy is not in reducing the number of CO_2 vibrational levels to 1224. In Fig. 14a, at the external edge of the boundary layer, a value close to the one obtained with TINA is found with the BL code, if the total enthalpy is computed by reducing the internal energy to the simple translational energy (curve 3).

To understand the role of the different internal energy terms in the enthalpy formula used in the state-to-state model, they are plotted in Fig. 14b. The highest contribution to the internal energy is given by the vibrational energy (curve 1 in Fig. 14b), and it is almost constant through the boundary layer. The translational energy (curve 4 of Fig. 14b) is slightly lower at the edge of the boundary layer; then, it decreases approaching the surface and, eventually, on the surface, it is near one order of magnitude lower than the vibrational energy. The

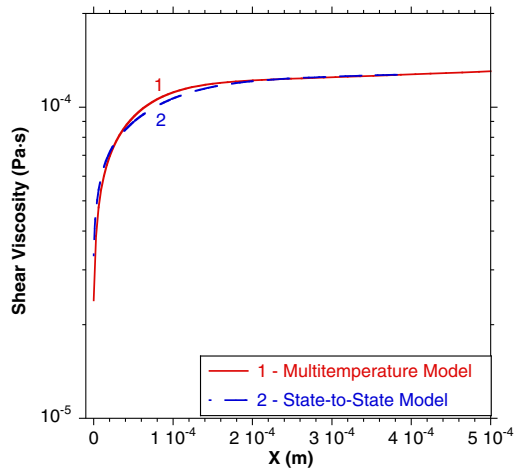


Fig. 13 Shear viscosity along the stagnation line, obtained with different models.

rotational energy (curve 2 of Fig. 14b) has the same trend of the translational energy, but it is lower since, in the BL code, it is approximated by kT , whereas the translational energy is calculated as $3/2 kT$. In Fig. 14b, to use a logarithmic scale, the inverse of the formation energy is plotted; in the neighbor of the surface, its absolute value overcomes the sum of the other terms so that the internal energy is negative, and the enthalpy too (see Fig. 14a). The formation energy is affected by the CO_2 formation energy more than by the other species ones; moreover, we have verified that, except in the region close to the surface, CO and O formation energies cancel each other.

Finally, the most important result to investigate is the heat flux; indeed, it can heavily affect both the design and the thermal protection system of an atmospheric probe. In Fig. 15, the different terms of the heat flux are reported, i.e., the fluxes caused by thermal conductivity (the Fourier flux) q_F , mass diffusion q_{MD} , thermal diffusion q_{TD} , and diffusion of vibrational energy transferred by excited molecules q_{DVE} (see Sec. II.A.2 and [7]) obtained by solving the BL code with the state-to-state kinetic and transport model described in Sec. II.A. The heat flux due to thermal diffusion, close to the surface, is of the same order as the Fourier flux; therefore, it plays an important role in the calculation of the total heat flux. On the other side, right on the surface, the mass diffusive flux drops to zero due to the noncatalytic boundary condition $(\partial C_v / \partial y)_w = 0$.

It is interesting to observe that the mass diffusion term seems in disagreement with the previous results of [8], obtained by solving the same boundary-layer equation system [Eqs. (12) and (13)] of the present paper. In particular, for the conditions $(\text{O}_2 + \text{O}) = 31.7\%$,

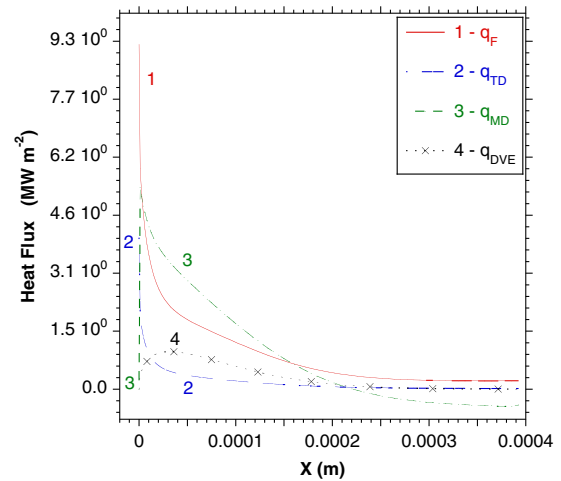


Fig. 15 Different contributions to the heat flux (Fourier, thermal diffusion, mass diffusion, diffusion of vibrational energy) along the normal to the surface (stagnation line). Results obtained with the BL code and the state-to-state model.

$\text{CO}_2 = 10.4\%$, $\text{CO} = 57.6\%$, $\text{C} = 0.3\%$, $T_w = 1500 \text{ K}$, $T_e = 6000 \text{ K}$, $P_e = 888 \text{ Pa}$, and $\beta = 2708 \text{ s}^{-1}$ (Test Case 4), the mass diffusion was almost zero; however, with respect to HYPULSE test case 1, the mixture is not exactly the same, the wall temperature is more than twice, and both P_e and β are a few order of magnitude lower. Moreover, in the present test case, the ratio P_e/β is almost equal to 1, whereas in the mentioned test case of [8], this ratio is about 0.33. All these reasons may lead to different behaviors of the mass diffusion flux.

To analyze the mass diffusion flux, we have run the boundary-layer code under the different sets of conditions reported in Table 1 (first, third, fourth, and fifth columns). The variation of mass fractions (not reported in this paper) in the boundary layer and the mass diffusion heat flux depend on the conditions themselves; moreover the higher is the variation of mass fractions, the higher the heat flux mass diffusion term is. In Fig. 16, the heat flux mass diffusion terms for the different test cases of Table 1 are plotted. When $P_e = 888 \text{ Pa}$ and $\beta = 2708 \text{ s}^{-1}$, the mass diffusive flux is almost zero (curves 2, 4), whereas if $P_e = 1.269 \times 10^5 \text{ Pa}$ and $\beta = 1.283 \times 10^5 \text{ s}^{-1}$, it is higher (curves 3 and 1): in particular, for $T_w = 1500 \text{ K}$ and $T_e = 6000 \text{ K}$, it reaches a maximum of $8.5710 \times 10^{-1} \text{ MW m}^{-1}$ at $\eta = 1.8 (X = 1.16 \times 10^{-4} \text{ m})$; and for $T_w = 700 \text{ K}$ and $T_e = 4555 \text{ K}$ (i.e., the HYPULSE test case), it reaches a maximum of 5.366 MW m^{-1} at $\eta = 0.08 (X = 1.21 \times 10^{-6} \text{ m})$, which is the first grid node after the surface.

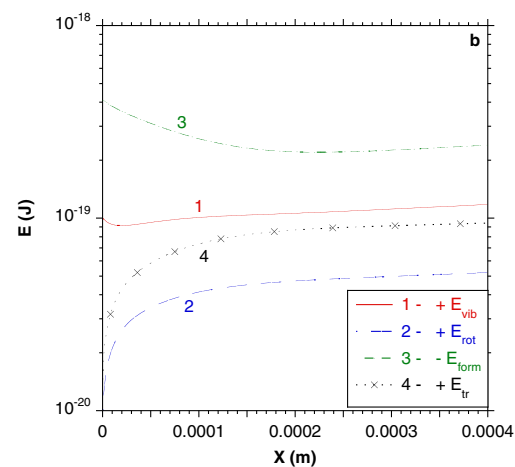
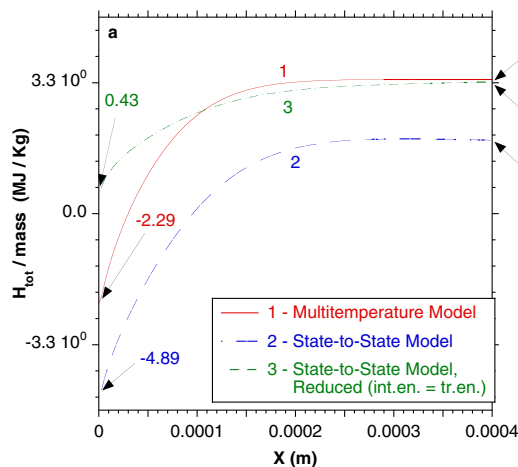


Fig. 14 Representations of a) enthalpy, obtained using different models; and b) vibrational, rotational, formation and translational energies, obtained using the state-to-state model (BL).

After the discussion on the different terms of the heat flux in the boundary layer obtained with the state-to-state model, it is really interesting to compare our results with the experimental values of the heat flux obtained by Hollis and Perkins [22,23] in the HYPULSE facility.

Remember that, in Fig. 10, the heat fluxes along the body surface obtained in the Hollis and Perkins [22,23] experiment and those calculated in the TINA CFD code, either with the Park et al. model [42] or with the multitemperature model for transport properties, are plotted. It should be emphasized that it was the flux near the surface and not along the normal to the surface; therefore, in Fig. 10, the point $y = 0$ corresponds to the stagnation point $\eta = X = 0$ in the BL code.

Let us now compare the experimental heat flux with the one calculated in the BL code using the state-to-state model. In the Hollis and Perkins [22,23] experiment the heat flux was not directly measured but, following three different schemes, it was derived by temperature measurements, then the only conductive component is taken into account; it is straightforward that the experimental heat flux must be compared with the thermal conduction (the Fourier) heat flux q_F calculated with the state-to-state model (Fig. 15, curve 1). The Fourier heat flux q_F on the surface, with its value of 9.1 MW/m^2 , falls into the range of the heat flux obtained by temperature measures in the Hollis and Perkins experiment (figure 16 of [23]), slightly overestimating the flux. Thus, our calculations confirm a good accuracy of the state-to-state kinetic and transport model for the heat flux predictions.

IV. Mars Pathfinder Entry Reconstruction

A. Computational Conditions

The geometry of the Mars Pathfinder aeroshell is shown in Fig. 17 [47]. For the Mars Pathfinder, using the base pressure measurements

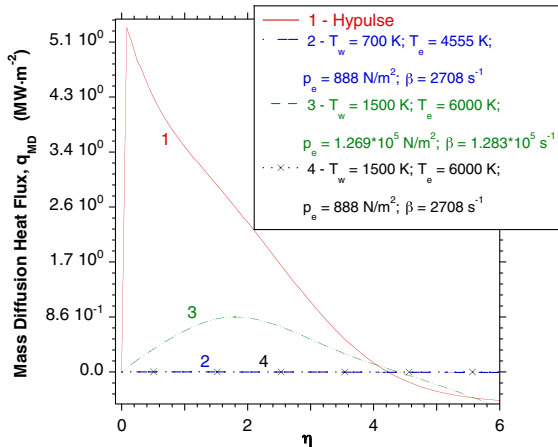


Fig. 16 Mass diffusion heat flux for different conditions. Results obtained with the BL code and the state-to-state model.

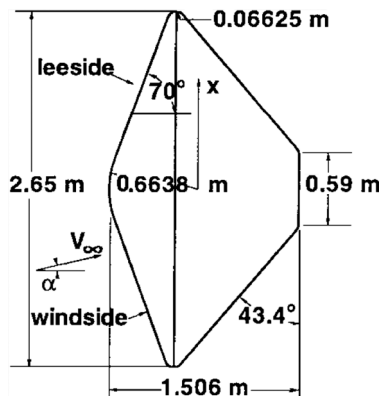


Fig. 17 Scheme of Mars Pathfinder [47].

Table 2 Test matrix for the numerical simulations of Mars Pathfinder entry

Case	Altitude, km	Velocity, m/s	Density, kg/m ³	Pressure, Pa	Temperature, K
Time 42	68.469	7490	1.01×10^{-5}	0.2462	129
Time 52	56.026	7364	5.76×10^{-5}	1.556	143
Time 66	41.204	6596	2.80×10^{-4}	8.941	169

from Viking, transition to turbulence occurred 7.5 s after peak heating [25]. As a consequence, the flow was considered to be laminar for the selected trajectory points reported in Table 2.

Axisymmetric computations have been performed using TINA for the Mars Pathfinder conditions reported in Table 2. Several meshes have been tested for checking the grid dependence of the results. A mesh with 100×80 cells has been found adequate, since attempts with finer meshes did not modify noticeably the results. The computational domain extends over 20 cm along the stagnation line, with a first cell of $10 \mu\text{m}$ at the wall in order to have a good accuracy when predicting the heating rate. The computational mesh is shown in Fig. 18.

The calculations have been carried out for an isothermal noncatalytic wall at 1500 K. The results have been converged with 200,000 iterations, and time steps were in between 0.1 and 1 times the CFL number, depending on the transport model (up to one for Blottner coefficients and 0.5 using the multitemperature model). The assumption of a laminar flow has been made, since transition to turbulence occurred after peak heating according to the analysis of the flight data [25]. The nonequilibrium thermochemical effects have been accounted through the Park et al. [42] and Kustova and Nagnibeda [13] models described in Sec. III.A.

B. Computational Results

Calculations have been carried out using the two different approaches already described for the trajectory points reported in Table 1. The flowfield distribution of the Mach number at 42 and 66 s are shown in Fig. 19. The shock standoff moves from 10 to 6 cm to the wall in 24 s. The pressure distribution at 66 s is plotted in Fig. 20. The flowfield distributions of the translational and vibrational temperatures along the trajectory are plotted in Figs. 21–23. The results show that the high shock-layer temperatures are encountered at the beginning of the entry with a strong thermal nonequilibrium at 42 s that decreases after. Such strong thermal nonequilibrium has already been observed in previous computations [44] carried out with different thermochemistry models. At peak heating (66 s), the level of translational temperature reaches a value in the range of 9000 K in the

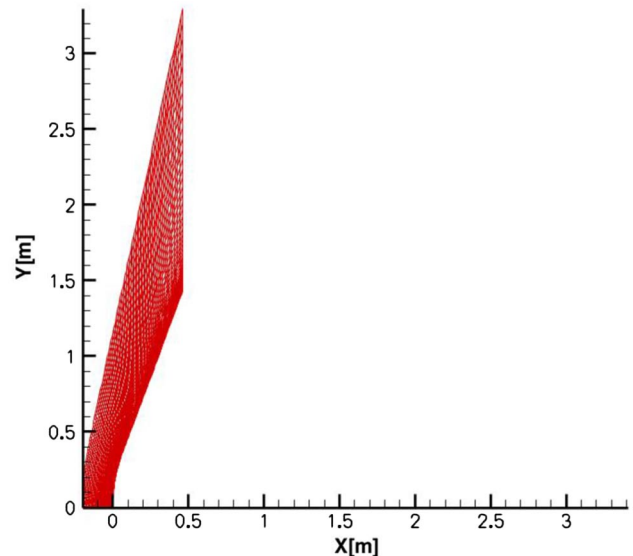


Fig. 18 Computational grid.

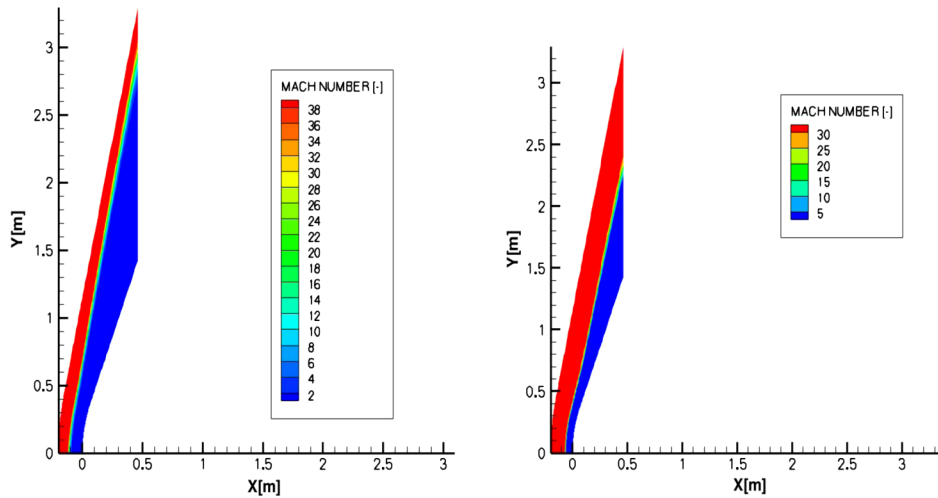


Fig. 19 Mach number distributions (Park et al. model [42]) at 42 and 66 s (left and right, respectively).

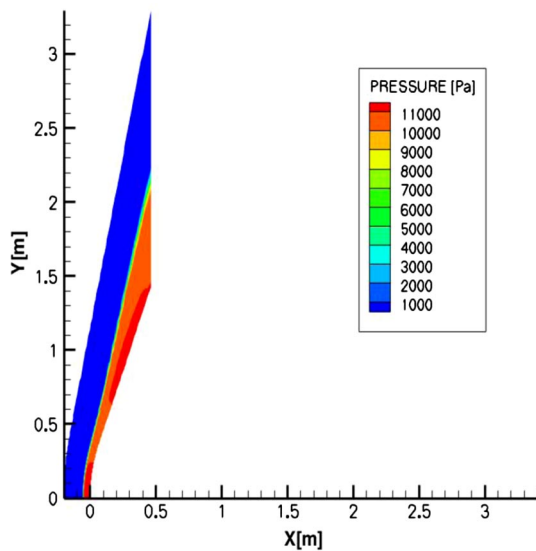


Fig. 20 Pressure distribution at 66 s (Park et al. model [42]).

shock layer, whereas the vibrational temperature is lower with 7000 K (see Fig. 23). No strong differences in the prediction of the temperature distribution can be noted when using the Kustova and

Nagnibeda [13] or Park et al. [42] models; the results are nearly similar.

No major difference has been observed in the species distributions computed using the two approaches. The mole fractions of CO_2 and CO predicted at 66 s are displayed in Fig. 24. As expected, CO_2 is nearly fully dissociated in the shock layer, which is translated by the high fraction of CO there. The maximum of the CO mole fraction is located at the frustum, where a part can be dissociated in the atomic species. The distribution of molecular oxygen predicted at peak heating is displayed in Fig. 25. The molecular oxygen is concentrated over a thin band at the shock location corresponding to the time required for its dissociation. The mole fraction of O_2 is higher in the region of the shock layer located near the shoulder due to the lower level of energy available.

Figure 26 shows the distribution of atomic oxygen during the entry; there is no drastic change in the distribution itself, and only the shape of the shock layer is modified due to the evolution of the shock standoff.

In Fig. 27, the mole fraction of atomic carbon at 42 and 66 s is displayed. The figure highlights that a low level of atomic carbon is present at the shock location with a higher fraction over the shoulder. The maximum of the carbon mole fraction decreases during entry: around a factor of two between 42 and 66 s. This is explained by the higher level of energy available at the beginning of the entry.

The stagnation point values of the convective heat flux predicted at the different trajectory points are reported in Table 3, together with

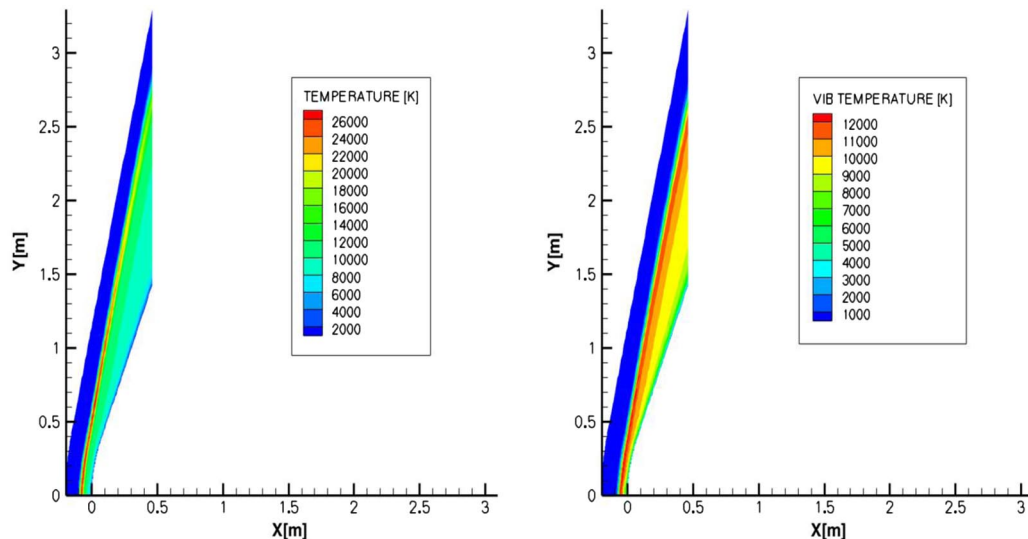


Fig. 21 Distributions of translational and vibrational temperatures obtained with the Kustova and Nagnibeda [13] model (left and right, respectively) at 42 s.

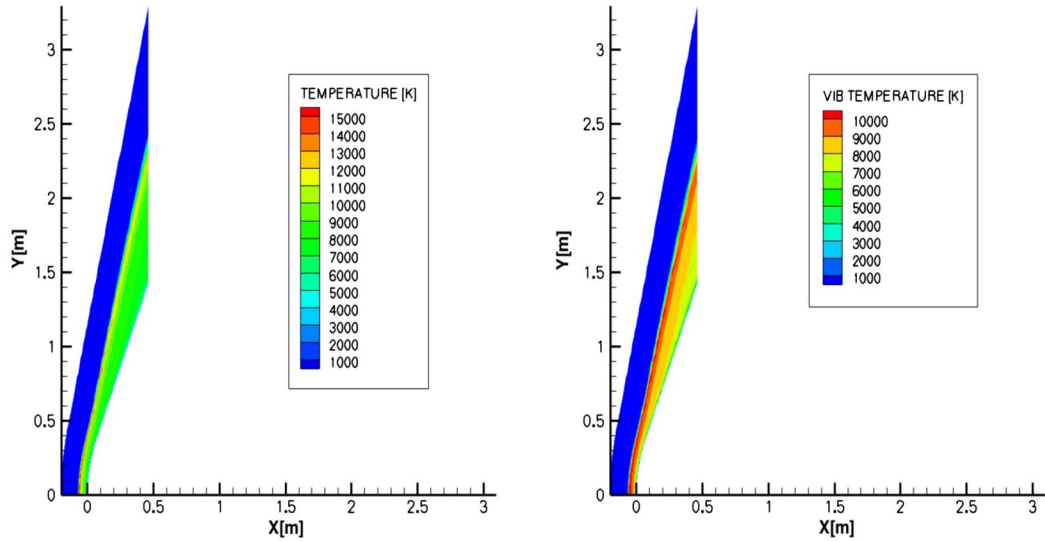


Fig. 22 Distributions of translational and vibrational temperatures obtained with the Kustova and Nagnibeda [13] model (left and right, respectively) at 52 s.

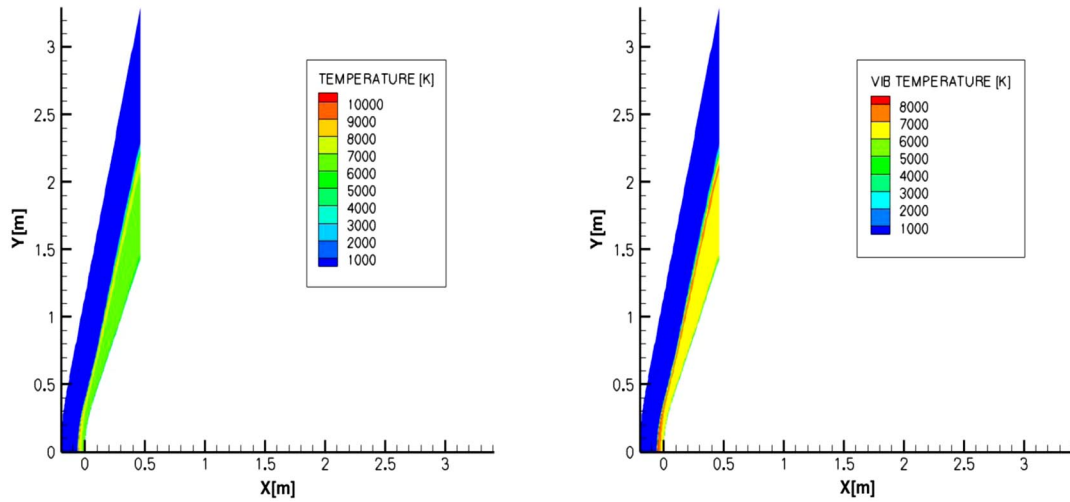


Fig. 23 Distributions of translational and vibrational temperatures obtained with the Kustova and Nagnibeda [13] model (left and right, respectively) at 66 s.

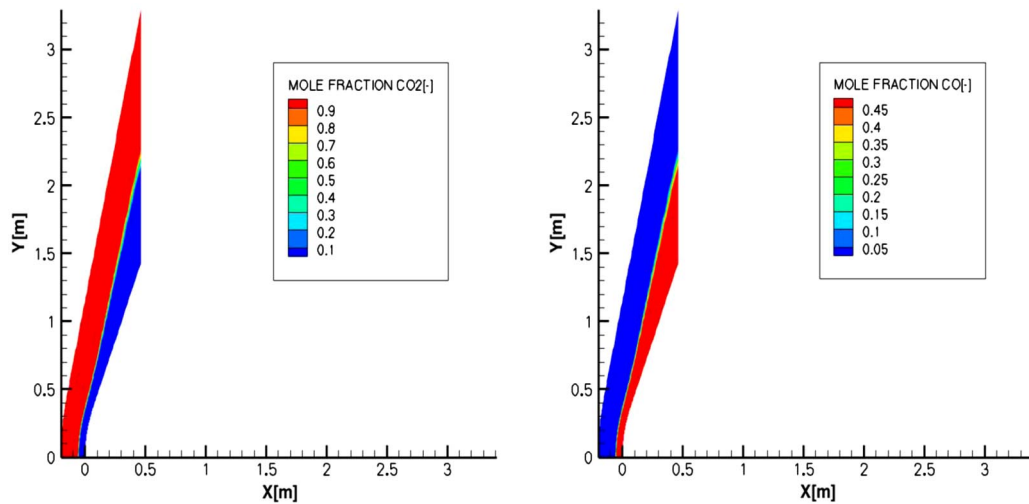


Fig. 24 Distributions of CO_2 and CO at 66 s obtained with the Park et al. [42] model (left and right, respectively).

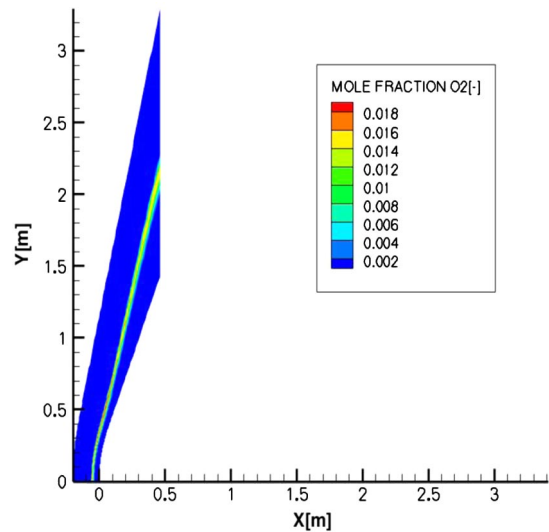


Fig. 25 Distributions of molecular oxygen obtained with the Park et al. [42] model at 66 s.

Table 3 Predicted convective heating at stagnation point and values from the literature

Time, s	Q (Park et al. [42]), kW/m ²	Q (Kustova and Nagnibeda [13]), kW/m ²	Q (Surzhikov and Omaly [28]), kW/m ²	Q (Milos et al. [25]), kW/m ²
42	57	67	— —	— —
52	191	225	— —	— —
66	308	355	≈250–300	≈400

some data from the literature [25,28]. From the current calculations, the same observation than for HYPULSE reconstruction can be done. The heat flux predicted using the Kustova and Nagnibeda [13] multitemperature model for the transport properties is higher than those obtained using the standard model. This difference is reflected in the dynamic viscosity, which is higher in the shock layer when using the Kustova and Nagnibeda model, as highlighted in Fig. 28. A good agreement with the literature data is obtained for the points at 52 and 66 s. Unfortunately, no value has been found for a noncatalytic heating at 42 s. The values computed by Surzhikov and Omaly [28] have been obtained for a noncatalytic wall at radiative equilibrium. The values of Milos et al. [25] have been computed using coupled

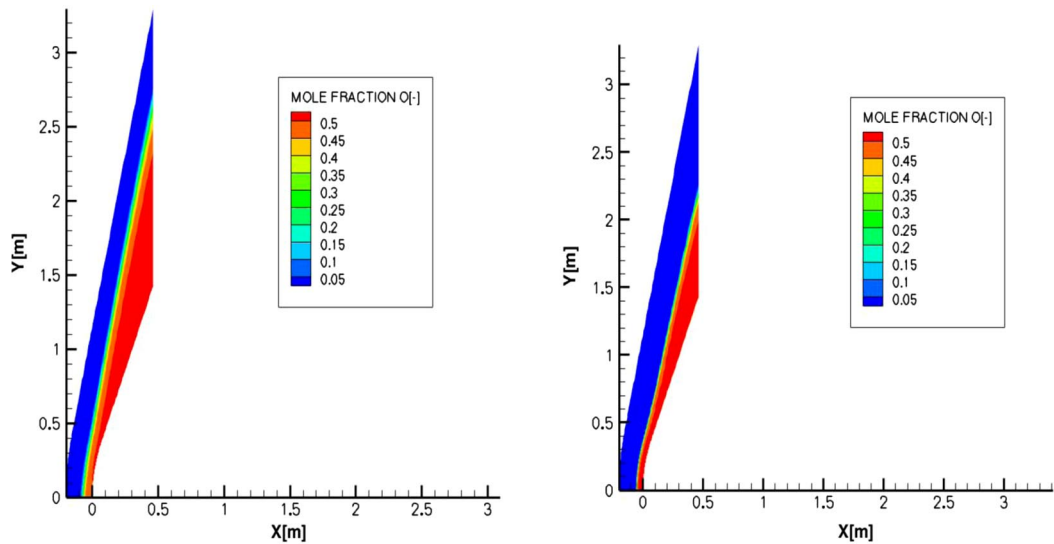


Fig. 26 Distributions of atomic oxygen obtained with the Park et al. [42] model at 42 and 66 s (left and right, respectively).

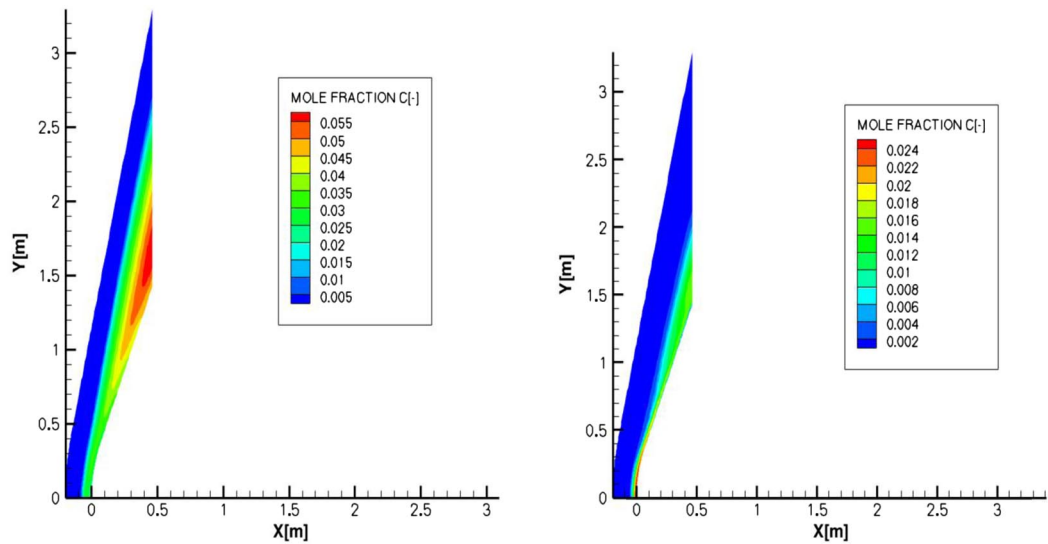


Fig. 27 Distributions of atomic carbon obtained with the Park et al. [42] model at 42 and 66 s (left and right, respectively).

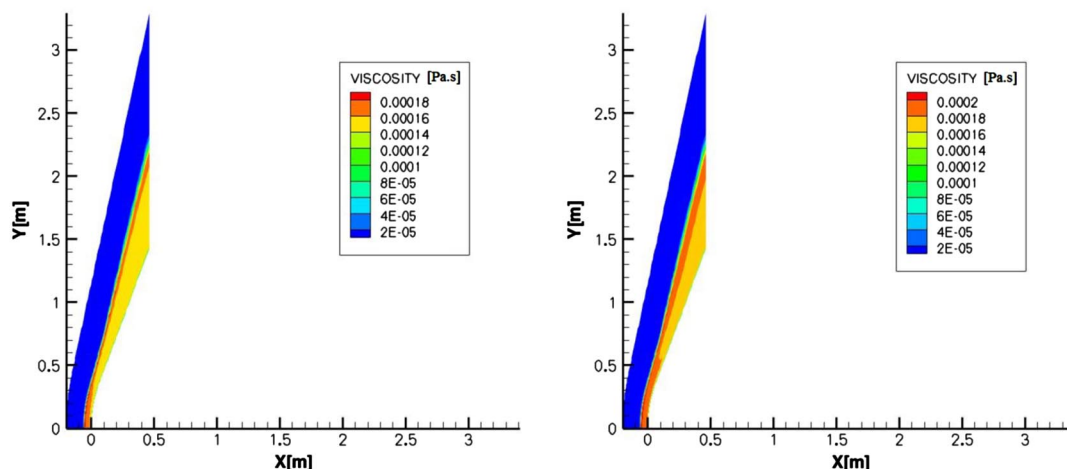


Fig. 28 Dynamic viscosity distributions predicted using Blottner et al.'s [34] and Kustova and Nagnibeda's [13] thermal properties (left and right, respectively) at peak heating.

calculations between CFD (with a noncatalytic wall) and material response codes.

V. Conclusions

Several sets of calculations using different approaches for computing the transport properties have been performed for the reconstruction of an experimental test case and different points along the Mars Pathfinder trajectory.

For the reconstruction of the test carried out in the HYPULSE facility, the numerical simulations show that the calculations carried out with the Kustova and Nagnibeda [13] multitemperature model achieve a better agreement for the heating predictions, since the experimental values are recovered in a large region of the model. The CFD calculations have been compared with boundary-layer predictions performed with a state-to-state model. The comparisons highlight a good agreement for the flowfield variables but some discrepancies for the prediction of the species mole fractions, especially close to the surface.

Three points along the Mars Pathfinder trajectory were computed for a noncatalytic wall. Again, the heating values obtained with the multitemperature model for the transport properties were in better agreement with the postflight calculations.

This demonstrates that a multitemperature approach is capable of describing the flow variables in the shock layer. The results show the interest of incorporating such models in CFD codes, since they are easier to implement. Additionally, their computational cost is moderate when compared to those induced by state-to-state models.

Acknowledgments

The research leading to these results has received funding from the European Community's Seventh Framework Programme (FP7/2007-2013) under grant agreement no. 242311. Partial support to E. Kustova by Saint Petersburg State University, through project 6.37.163.2014, and the Russian Foundation for Basic Research, grant 15-08-03371, is also acknowledged. Partial support to I. Armenise by Ministero dell'Istruzione, dell'Università e della Ricerca (MIUR) through Progetti di Rilevante Interesse Nazionale (PRIN), project 2010ERFKXL_007 is also acknowledged. This paper was already partially presented at the 6th International Workshop on Radiation of High Temperature Gases in Atmospheric Entry, held at St. Andrews, Scotland, United Kingdom, 24–28 November 2014.

References

- [1] Reynier, P., "Survey of Aerodynamics and Aerothermodynamics Efforts Carried Out in the Frame of Mars Exploration Projects," *Progress in Aerospace Sciences*, Vol. 70, Oct. 2014, pp. 1–27. doi:10.1016/j.paerosci.2014.03.004
- [2] "Historical Log," NASA Mars Exploration [online database], <http://mars.nasa.gov/programmissions/missions/log/> [retrieved 2015].
- [3] Wright, M. J., Olejniczak, J., Brown, J. L., Hornung, H. G., and Edquist, K. T., "Modeling of Shock Tunnel Aeroheating Data on the Mars Science Laboratory Aeroshell," *Journal of Thermophysics and Heat Transfer*, Vol. 20, No. 4, 2006, pp. 641–651. doi:10.2514/1.19896
- [4] Rouzaud, O., Tessé, L., Soubrié, T., Soufiani, A., Rivière, P., and Zeitoun, D., "Influence of Radiative Heating on a Martian Orbiter," *Journal of Thermophysics and Heat Transfer*, Vol. 22, No. 1, 2008, pp. 10–19. doi:10.2514/1.28259
- [5] Mahzari, M., and Braun, R. D., "Time-Dependent Mars Entry Aeroheating Estimation from Simulated In-Depth Heat Shield Temperature Measurements," *Journal of Thermophysics and Heat Transfer*, Vol. 27, No. 3, 2013, pp. 435–446. doi:10.2514/1.T3986
- [6] Kustova, E., and Nagnibeda, E., "State-to-State Theory of Vibrational Kinetics and Dissociation in Three-Atomic Gases," *AIP Conference Proceedings*, Vol. 585, Aug. 2001, pp. 620–627. doi:10.1063/1.1407618
- [7] Armenise, I., and Kustova, E. V., "State-to-State Models for CO₂ Molecules: From the Theory to an Application to Hypersonic Boundary Layers," *Chemical Physics*, Vol. 415, March 2013, pp. 269–281. doi:10.1016/j.chemphys.2013.01.034
- [8] Armenise, I., and Kustova, E. V., "On Different Contributions to the Heat Flux and Diffusion in Non-Equilibrium Flows," *Chemical Physics*, Vol. 428, Jan. 2014, pp. 90–104. doi:10.1016/j.chemphys.2013.11.003
- [9] Armenise, I., Capitelli, M., and Gorse, C., "Nitrogen Nonequilibrium Vibrational Distributions and Non-Arrhenius Dissociation Constants in Hypersonic Boundary Layers," *Journal of Thermophysics and Heat Transfer*, Vol. 12, No. 1, 1998, pp. 45–51. doi:10.2514/2.6300
- [10] Armenise, I., Capitelli, M., and Gorse, C., "Nonequilibrium Vibrational Kinetics of Air Hitting a Catalytic SiO₂ Surface," *Journal of Spacecraft and Rockets*, Vol. 38, No. 4, 2001, pp. 482–487. doi:10.2514/2.3730
- [11] Armenise, I., Barbato, M., Capitelli, M., and Gorse, C., "Surface Recombination Coefficients and Boundary-Layer Hypersonic-Flows Calculations on Different Surfaces," *Journal of Spacecraft and Rockets*, Vol. 41, No. 2, 2004, pp. 310–313. doi:10.2514/1.9202
- [12] Taylor, R., and Bitterman, S., "Survey of Vibrational Relaxation Data for Process Important in the CO₂-N₂ Laser System," *Reviews of Modern Physics*, Vol. 41, No. 1, 1969, pp. 26–47. doi:10.1103/RevModPhys.41.26
- [13] Kustova, E., and Nagnibeda, E., "On a Correct Description of a Multitemperature Dissociating CO₂ Flow," *Chemical Physics*, Vol. 321, No. 3, 2006, pp. 293–310. doi:10.1016/j.chemphys.2005.08.026
- [14] Kustova, E., and Nagnibeda, E., "Kinetic Model for Multi-Temperature Flows of Reacting Carbon Dioxide Mixture," *Chemical Physics*, Vol. 398, No. 1, 2012, pp. 111–117. doi:10.1016/j.chemphys.2011.05.019

- [15] Likalter, A., "On the Vibrational Distribution of Polyatomic Molecules," *Prikladnaia Mekhanika i Tekhnicheskaya Fizika*, Vol. 4, 1976, p. 3 (in Russian).
- [16] Cenian, A., "Study of Non-Equilibrium Vibrational Relaxation of CO₂ Molecules During Adiabatic Expansion in a Supersonic Nozzle. The Treanor Distribution—Existence and Generation," *Chemical Physics*, Vol. 132, Nos. 1–2, 1989, pp. 41–48.
doi:10.1016/0301-0104(89)80076-X
- [17] Kustova, E., and Nagnibeda, E., "Non-Equilibrium Distributions in CO₂ and Their Influence on the Transport and Thermodynamic Properties," *Rarefied Gas Dynamics*, edited by Brun, R., Cepadues, Vol. 2, Toulouse, France, 1999, pp. 289–296.
- [18] Chikhaoui, A., and Kustova, E., "Effect of Strong Excitation of CO₂ Asymmetric Mode on Transport Properties," *Chemical Physics*, Vol. 216, No. 3, 1997, pp. 297–315.
doi:10.1016/S0301-0104(97)00017-7
- [19] Kustova, E., Nagnibeda, E., Shevelev, Y., and Syzranova, N., "Nonequilibrium Supersonic CO₂ Flows with Real Gas Effects near a Blunt Body," *AIP Conference Proceedings*, Vol. 1084, Dec. 2009, pp. 831–836.
- [20] Kustova, E., Nagnibeda, E., Shevelev, Y., and Syzranova, N., "Comparison of Different Models for Non-Equilibrium CO₂ Flows in a Shock Layer near a Blunt Body," *Shock Waves*, Vol. 21, No. 3, 2011, pp. 273–287.
doi:10.1007/s00193-011-0324-0
- [21] TINA Version 4 Theory and User Manual, TN89/96 No. 7, Fluid Gravity Engineering, Emsworth, England, U.K., March 2008.
- [22] Hollis, B. R., and Perkins, J. N., "Hypervelocity Aeroheating Measurements in Wake of Mars Mission Entry Vehicle," *26th AIAA Fluid Dynamics Conference*, AIAA Paper 1995-2314, June 1995.
- [23] Hollis, B. R., and Perkins, J. N., "High-Enthalpy Aerothermodynamics of a Mars Entry Vehicle. Part 1: Experimental Results," *Journal of Spacecraft and Rockets*, Vol. 34, No. 4, July–Aug. 1997, pp. 449–456.
doi:10.2514/2.3257
- [24] Beck, J., Tran, P. H., and Walpot, L., "Aerothermodynamics of the ExoMars Entry Demonstrator Module," *7th European Aerothermodynamic Symposium*, ESA SP-692, May 2011.
- [25] Milos, F. S., Chen, Y.-K., Congdon, W. M., and Thomas, J. M., "Mars Pathfinder Entry Temperature Data, Aerothermal, and Heatshield Material Response," *Journal of Spacecraft and Rockets*, Vol. 36, No. 3, May–June 1999, pp. 380–391.
doi:10.2514/2.3457
- [26] Chen, Y.-K., Henline, W. D., and Tauber, M. E., "Mars Pathfinder Trajectory Based Heating and Ablation Calculations," *Journal of Spacecraft and Rockets*, Vol. 32, No. 2, 1995, pp. 225–230.
doi:10.2514/3.26600
- [27] Paterna, D., Monti, R., Savino, R., and Esposito, A., "Experimental and Numerical Investigation of Martian Atmospheric Entry," *Journal of Spacecraft and Rockets*, Vol. 39, No. 2, March–April 2002, pp. 227–236.
doi:10.2514/2.3804
- [28] Surzhikov, S., and Omal, P., "Radiative Gas Dynamics of Martian Space Vehicles," *49th AIAA Aerospace Sciences Meeting*, AIAA Paper 2011-0452, Jan. 2011.
- [29] Surzhikov, S., "Comparative Analysis of Radiative Aerothermodynamics of Martian Entry Probes," *43rd AIAA Thermophysics Conference*, AIAA Paper 2012-2867, June 2012.
- [30] Beck, J., and Lynn, S., "Modelling of CO₂ Thermochemistry," *Fluid Gravity Engineering*, Rept. CR080/07, Emsworth, England, U.K., Dec. 2007.
- [31] Anderson, J. D., Jr., *Hypersonic and High Temperature Gas Dynamics*, Series in Aeronautical and Aerospace Engineering, McGraw-Hill, New York, 1989, pp. 213–259, 611–636.
- [32] Yee, H. C., "Construction of Explicit and Implicit Symmetric TVD Schemes and Their Applications," *Journal of Computational Physics*, Vol. 68, No. 1, 1987, pp. 151–179.
doi:10.1016/0021-9991(87)90049-0
- [33] Wilke, C. R., "A Viscosity Equation for Gas Mixture," *Journal of Chemical Physics*, Vol. 18, No. 4, 1950, pp. 517–519.
doi:10.1063/1.1747673
- [34] Blottner, F. G., "Chemically Reacting Viscous Flow Program For Multi-Component Gas Mixtures," Sandia Labs. Rept. SC-RR-70-754, Albuquerque, NM, Dec. 1971.
- [35] Mazoué, F., and Marraffa, L., "Flow-Field/Radiation Coupling Analysis for Huygens Probe entry into Titan Atmosphere," AIAA Paper 2005-5392, 2005.
- [36] Merrifield, J. A., and Fertig, M., "Radiation-Flowfield Coupling Solutions for the FIRE-II Flight Experiment," *Proceedings of 3rd International Workshop on Radiation and High Temperature Gases in Atmospheric Entry* [CD-ROM], Heraklion, Greece, Sept.–Oct. 2008; also ESA SP-667, Jan. 2009.
- [37] Mazoué, F., and Reynier, P. H., "Predictions of Radiative and Convective Fluxes at Stagnation Point for Earth High-Speed Re-Entry," *Proceedings of 3rd International Workshop on Radiation and High Temperature Gases in Atmospheric Entry* [CD-ROM], Heraklion, Greece, Sept.–Oct. 2008; also ESA SP-667, Jan. 2009.
- [38] Hollis, B. R., and Perkins, J. N., "High-Enthalpy Aerothermodynamics of a Mars Entry Vehicle. Part 2: Computational Results," *Journal of Spacecraft and Rockets*, Vol. 34, No. 4, July–Aug. 1997, pp. 457–463.
doi:10.2514/2.3258
- [39] Hollis, B. R., and Perkins, J. N., "Comparison of Experimental and Computational Aerothermodynamics of a 70 deg Sphere-Cone," *31st AIAA Thermophysics Conference*, AIAA Paper 1996-1867, June 1996.
- [40] Hollis, B. R., "Experimental and Computational Aerothermodynamics of a Mars Entry Vehicle," Ph.D. Thesis, Univ. of Raleigh, Raleigh, NC, Dec. 1996.
- [41] Candler, G. V., "Computation of Thermo-Chemical Nonequilibrium Martian Atmospheric Entry Flows," AIAA Paper 1990-1695, June 1990.
- [42] Park, C., Howe, J. T., Jaffe, R. L., and Candler, G. V., "Review of Chemical Problems of Future NASA Missions. Part II: Mars Entries," *Journal of Thermophysics and Heat Transfer*, Vol. 8, No. 1, Jan.–March 1994, pp. 9–23.
doi:10.2514/3.496
- [43] Bultel, A., *Elaboration de Codes-Modèles Collisionnels-Radiatifs Électroniques Spécifiques Portant sur CO et CO₂*, Rapport de Contrat, CORIA, Rouen, Sept. 2009.
- [44] Reynier, P. H., Lino da Silva, M., Marraffa, L., and Mazoué, F., "Preliminary Study of Mars Entry: Application to the Prediction of Radiation," *Proceedings of the 2nd International Radiation Workshop*, ESA SP-533, Porquerolles, France, Oct. 2004.
- [45] Bruno, D., Capitelli, M., Esposito, F., Longo, S., and Minelli, P., "Direct Simulation of Non-Equilibrium Kinetics Under Shock Conditions in Nitrogen," *Chemical Physics Letters*, Vol. 360, Nos. 1–2, 2002, pp. 31–37.
doi:10.1016/S0009-2614(02)00772-8
- [46] Edquist, K. T., Hollis, B. R., Johnston, C. O., Bose, D., White, T. R., and Mahzari, M., "Mars Science Laboratory Heatshield Aerothermodynamics: Design and Reconstruction," *44th AIAA Thermophysics Conference*, AIAA Paper 2013-2781, June 2013.
- [47] Gnoffo, P. A., Weilmuenster, K. J., Braun, R. D., and Cruz, C. I., "Effects of Sonic Line Transition on Aerothermodynamics of the Mars Pathfinder Probe," AIAA Paper 1995-1825, 1995.